

Effect of the Ligand Structure on Chemical Vapor Deposition of WN_xC_y Thin Films from Tungsten Nitrido Complexes of the Type $WN(NR_2)_3$

Arijit Koley,^{†,||} Christopher T. O'Donohue,^{‡,||} Michelle M. Nolan,[†] K. Randall McClain,[†] Richard O. Bonsu,[†] Roman Y. Korotkov,[§] Tim Anderson,[‡] and Lisa McElwee-White^{*,†}

[†]Department of Chemistry, University of Florida, Gainesville, Florida 32611-7200, United States

[‡]Department of Chemical Engineering, University of Florida, Gainesville, Florida 32611-6005, United States

[§]Arkema Inc., 900 First Avenue, King of Prussia, Pennsylvania 19406, United States

Supporting Information

ABSTRACT: Tungsten nitrido complexes of the type $WN(NR_2)_3$ [NR_2 = combinations of NMe_2 , NEt_2 , N^iPr_2 , N^nPr_2 , N^tBu_2 , piperidine, and azepane] were synthesized as precursors for aerosol-assisted chemical vapor deposition of WN_xC_y thin films. The effects of the amido substituents on precursor volatility and decomposition were evaluated experimentally and computationally. Films deposited using $WN(NMe_2)(N^iPr_2)_2$ as a single-source precursor were assessed as diffusion barrier materials for Cu metallized integrated circuits in terms of growth rate, surface roughness, composition, and density. In diffusion barrier tests, Cu (~100 nm)/ WN_xC_y (~5 nm)/Si samples prepared from $WN(NMe_2)(N^iPr_2)_2$ were annealed for 30 min at 500 °C and successfully blocked Cu penetration according to four-point probe, X-ray diffraction, scanning electron microscopy etch-pit test, and high-resolution transmission electron microscopy measurements.



INTRODUCTION

The manufacture of integrated circuits requires deposition of diffusion barrier material to prevent the migration of Cu and its incorporation into Si and penetration into high-porosity low- κ dielectrics. Cu diffusion can increase contact resistances, produce contact layer embrittlement, promote delamination from low- κ materials, and generate energy levels within the band gap of Si that act as recombination centers.¹ Currently, a physical vapor deposited Ta/TaN bilayer structure is used,² but with the miniaturization of feature sizes, physical vapor deposition (PVD) has been projected to become inadequate due to conformality issues deriving from the highly directional nature of deposition. Chemical vapor deposition (CVD) and atomic layer deposition (ALD) are candidates to succeed PVD technologies. Among materials considered for diffusion barrier applications are transition metal nitrides and carbonitrides,^{3–6} and more recently self-forming barriers (e.g., $MnSi_xO_y$).^{7–10} WN_xC_y has been discussed as a possible candidate given its low resistivity, thermal and mechanical stability, resistance to recrystallization, ease of processing, and adhesion to and compatibility with current integrated circuit (IC) materials.^{6,11}

We have been using the CVD of WN_xC_y as a platform to examine mechanism-based design of single-source precursors^{12,13} featuring tungsten complexes with nitrogen-coordinated ligands such as imido, guanidinate, amidinate, amido, and hydrazido moieties.^{12,14} One focus of this work has been lowering the deposition temperature (<350 °C)^{15–21} to decrease damage to adjoining thermally sensitive dielectric

layers²² or contact level structures.^{23,24} Identification of cleavage of the N–C bond as the rate-determining step in deposition of WN_xC_y from the imido complexes $Cl_4(CH_3CN)WNR$ ($R = Ph, ^iPr, allyl$)²⁵ suggested a precursor design strategy in which the N–C bond was replaced by a weaker N–N bond. The result was a lowering of the deposition temperatures from the 400–500 °C range obtained with imido complexes^{26–28} to the 250–300 °C range observed for the analogous hydrazido complexes.²⁹ Elimination of that bond by moving to a terminal nitrido ligand instead of imido or hydrazido ligands was the next step in the evolving precursor design.^{30,31}

We then reported the synthesis of the nitrido complex $WN(NMe_2)_3$ (**1**) and the resulting CVD of WN_x nanospheres³⁰ and WN_xC_y thin films³¹ from **1** at temperatures as low as 75 and 125 °C, respectively. We have also investigated the CVD of WN_xC_y thin films from $WN(NEt_2)_3$ (**2**) at temperatures as low as 100 °C and demonstrated their viability as Cu diffusion barriers at 5.5 nm thickness when annealed for 30 min at 500 °C.³² We now report the syntheses of additional complexes of the type $WN(NR_2)_3$, the results of prescreening these complexes as possible CVD precursors, and growth of WN_xC_y thin films at temperatures as low as 100 °C from $WN(NMe_2)(N^iPr_2)_2$ (**3**).

Received: September 20, 2015

Revised: November 10, 2015

Published: November 13, 2015

RESULTS AND DISCUSSION

Precursor Design and Synthesis. Complexes 1–4 (Figure 1) were prepared as previously reported.^{30,31} Since

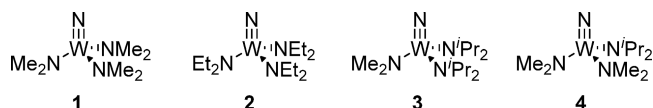
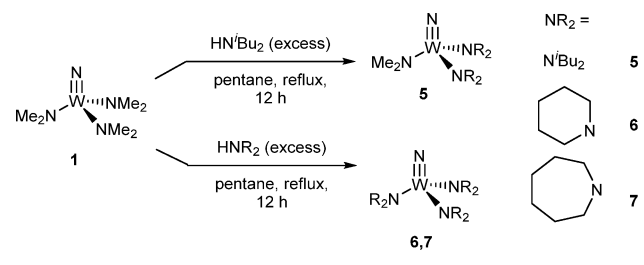


Figure 1. Structures of complexes 1–4.

volatility of the complexes is important for application in CVD and ALD, the vapor-phase transport of these complexes was tested by sublimation. In these studies, 3 and 4 were found to be more volatile than 1 and 2, despite their higher molecular weights. The increase in volatility in going from homoleptic ligand sets to heteroleptic ones has been previously noted and ascribed to perturbation of crystal packing forces by lowered symmetry.^{12,33,34} It has also been postulated that steric bulk around the metal center contributes to volatility by hindering intermolecular interactions. The higher volatility of 3 and 4 led us to synthesize additional complexes containing heteroleptic sets of ligands, in which the lowered symmetry is complemented by varying degrees of steric bulk in the dialkylamide ligands.

The isobutyl derivative 5 was synthesized by refluxing 1 with excess diisobutylamine in pentane for 12 h (Scheme 1).

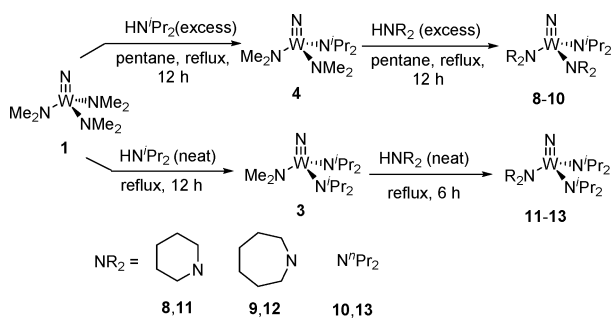
Scheme 1. Synthesis of 5–7



Reaction of 1 with excess piperidine or azepane under the same reaction conditions resulted in replacement of all three NMe₂ ligands to afford 6 or 7. This is most likely due to the smaller cone angles of cyclic secondary amines such as piperidine and azepane when compared to diisopropylamine and diisobutylamine.³⁵

Compounds 8–13 were synthesized from 1 in a one-pot strategy which takes advantage of the steric demand of the NⁱPr₂ ligand to limit the extent of substitution in the presence of excess diisopropylamine (Scheme 2). In refluxing pentane,

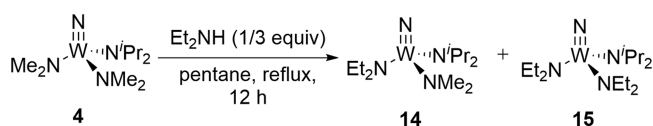
Scheme 2. Synthesis of 8–13



only a single substitution to generate complex 4 is possible. At the higher temperature of refluxing diisopropylamine, a second substitution affords 3 as the intermediate. Subsequent addition of a different amine to either 3 or 4 results in formation of 8–13.

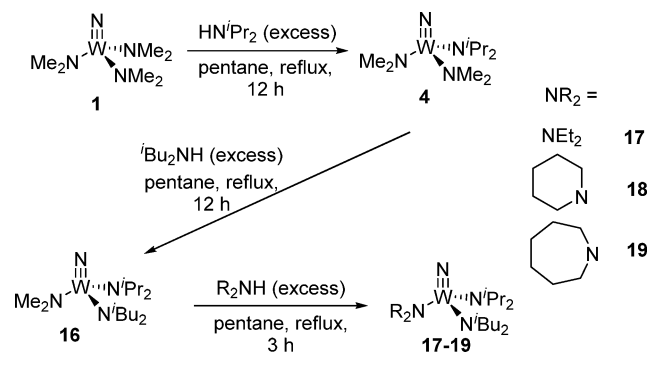
Attempts to synthesize the unsymmetrical complex 14 by controlling the stoichiometry of less sterically hindered amines were unsuccessful. Reflux of 4 with 1/3 equiv of diethylamine in pentane resulted in the formation of a mixture of 14 and 15 (Scheme 3). Efforts to separate 14 and 15 through extraction, crystallization, or sublimation did not provide a pure sample of either product.

Scheme 3. Synthesis of 14 and 15



The alternative unsymmetrical target complex 16, which contains the more sterically demanding diisobutylamide ligand in place of the diethylamido ligand of 14 could be prepared by a one-pot synthesis strategy (Scheme 4) that affords 16 in 50%

Scheme 4. Synthesis of 16–19

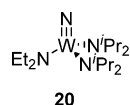


yield. Further substitutions of the dimethylamido ligand in 16 could be obtained by reaction with excess diethylamine, piperidine, and azepane in refluxing pentane to obtain 17, 18, and 19, respectively.

Structural Effects on Precursor Volatility. The effect of substituent choice on the volatility and thermal stability of complexes 5–19 was assessed by sublimation. Complex 5 contains NR₂ groups that have a cone angle (138° for NⁱBu₂) nearly identical to that of the NR₂ groups of 3 (137° for NⁱPr₂)³⁵ but are of higher molecular weight. Precursor 5 was found to be less volatile than 3 (Table 1), suggesting that, as expected, the lower molecular weight of the isopropyl derivative 3 dominates volatility when the steric profiles are similar. Reduced symmetry about the metal center also has the expected effect on precursor volatility.^{12,33,34} Homoleptic complexes 6 and 7 have volatilities (as measured by the sublimation temperature) that are similar to that of 2, whereas heteroleptic complexes 8–13 were similar to 3, 4, and the previously reported complexes 15 and 20 (Figure 2).³¹ The highest volatilities were found for the unsymmetrical complexes 16–19, which all sublimed at temperatures below 50 °C at 150–200 mTorr (Table 1).

Table 1. Sublimation Conditions and Compound Recovery for 1–13 and 15–20

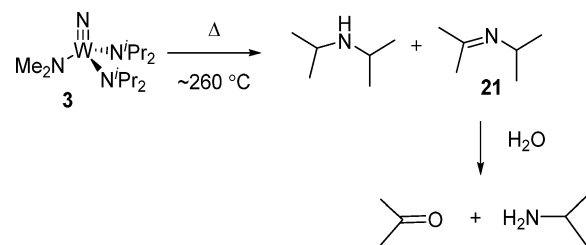
compd	pressure (mTorr)	T (°C)	recovery (%)	ref
1	150–250	90–105	55	30
2	150–250	75–80	55	31
3	350–450	65–70	40	31
4	350–450	65–70	35	31
5	150–250	80–85	40	this work
6	150–250	70–80	45	this work
7	150–250	75–85	40	this work
8	150–250	60–70	45	this work
9	150–250	70–80	35	this work
10	150–250	65–70	55	this work
11	150–250	55–65	40	this work
12	150–250	60–65	35	this work
13	200–300	50–55	35	this work
15	250–350	62–68	30	31
16	150–250	45–55	55	this work
17	150–250	40–50	60	this work
18	150–250	42–50	50	this work
19	150–250	42–50	45	this work
20	250–350	58–68	30	31

**Figure 2.** Structure of complex 20.

Thermogravimetric analysis (TGA) of 3 (Figure S-3) is consistent with sublimation of the compound at approximately 230 °C at atmospheric pressure. This result confirms that complex 3 is sufficiently stable to survive the reduced pressure sublimation described in Table 1. In contrast, some of the precursors, such as 4, could not be sublimed at atmospheric pressure because their decomposition temperatures were too low. See Figure S-3 in the Supporting Information for the TGA of 4, for which decomposition is competitive with atmospheric pressure sublimation.

Thermolysis of Neat 3. Thermolysis of 3 was performed to identify the volatile byproducts of its decomposition and provide information on possible reaction pathways for deposition of WN_xC_y . To obtain samples of the pyrolysis products, complex 3 was heated to ~260 °C under 1 atm of argon and the condensate was collected at -78 °C. A brown-black residue was left after thermolysis. GC–EI MS of the condensate confirmed the presence of the pyrolysis product diisopropylamine. Also detected in the mass spectra were imine 21, isopropylamine, and acetone. The isopropylamine and acetone are the products of hydrolysis of 21 by adventitious water introduced into the sample during trapping and handling (Scheme 5).

Computational Study of the Gas-Phase Decomposition of 3. A computational study was carried out to explore possible mechanistic pathways leading to loss of diisopropylamine, a thermolysis product of 3 (Scheme 5). For the lowest energy gas-phase pathway that was located (Figure 3), the first step is unimolecular β -proton abstraction by the adjacent amide, which occurs via a relatively high energy transition state ($\Delta G^\ddagger = 40.2$ kcal/mol; $\Delta H^\ddagger = 39.2$ kcal/mol). Formation of INT1 is followed by the coordination of another molecule of 3 to generate the bimetallic INT2 in a slightly exothermic step.

Scheme 5. Thermolysis of 3

Although the transition state linking INT1 to INT2 could not be located computationally, addition of 3 to the coordinatively unsaturated INT1 likely has a very low barrier. Likewise, the transition state from INT2 to INT3 was not located, but loss of diisopropylamine from the sterically crowded INT2 is also likely to have a moderately low barrier. Attempts to locate pathways in which two molecules of 3 reacted directly in the gas phase were unsuccessful. The inability to locate a bimolecular pathway is in contrast to computational results on the less sterically hindered dimethylamido complex 1,³¹ for which bimolecular gas-phase reaction was preferred over the unimolecular pathway. In a related pathway involving the decomposition of $WN(NEt_2)_3$ (Figure S-1, Supporting Information), the energy barrier for formation of the bimolecular transition state (TS2) and the energy barrier for the subsequent step involving elimination of amine (INT2) are isoenergetic ($\Delta\Delta G = 0.3$ kcal/mol).

WN_xC_y Film Growth. An Arrhenius plot of the film growth kinetics for depositions using 3 (Figure 4) dissolved in pyridine (aerosol-assisted chemical vapor deposition, AACVD) showed three growth regimes: a kinetically limited regime at low temperatures with an apparent activation energy of 0.330 ± 0.016 eV, a mass transfer limited regime, and a parasitic reaction regime at high temperatures. As shown in Figure 4, this behavior is different from that observed in depositions using 1 and 2 where only two growth regimes exist: mass transfer limited and parasitic reaction. Apparently, the low-temperature surface deposition reactions for 1 and 2 are faster than the mass transfer rates. Conversely, the observation of a low-temperature kinetic limitation using 3 indicates the rate-limiting reaction step is slower than the mass transfer rate in the lower temperature range. The greater steric bulk of 3 (vs 1 and 2) and the computational evidence for bimolecular decomposition steps are consistent with a greater kinetic limitation for film growth from 3 at low temperatures. This kinetic barrier, however, is still small for typical CVD conditions where apparent activation energies are normally above 0.5 eV.³⁶ It has previously been argued that the lowest energy pathway for film deposition is most likely the result of intermolecular interactions between surface-bound species or a surface–gas species interaction.^{30,31}

In the mass transfer limited regime, there is a noticeable difference in growth rate among the precursors, with the average growth rate increasing as $1 < 3 < 2$. In general, growth rate temperature dependence under mass transfer limited conditions follows a power law, T^n , where n is typically 1.7–1.8 for a vertical down flow design.²⁵ Depositions using 1, 2, and 3 exhibit values of 1.3, 2.1, and 2.0 for n , respectively. A value of 2.1 has been previously reported for a different precursor in the same reactor.³⁷

At higher deposition temperatures (>400 °C), the growth rates from 1, 2, and 3 decrease with increasing temperature.

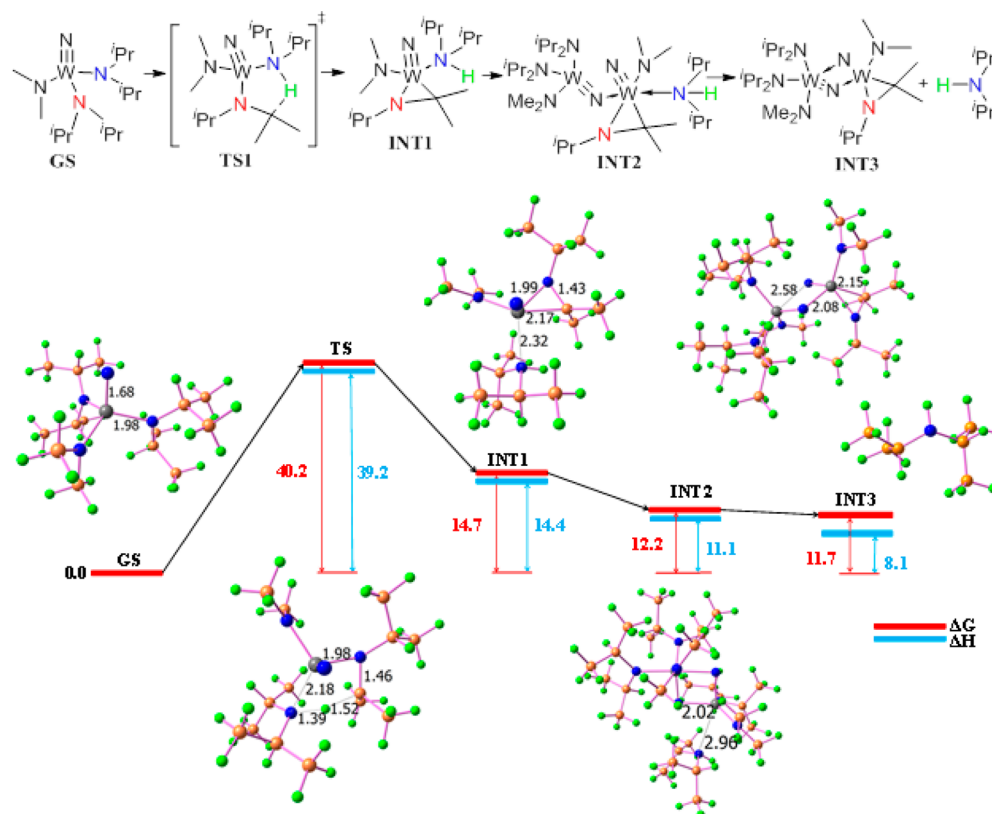


Figure 3. Calculated reaction surface (ΔG and ΔH , kcal mol⁻¹) for gas-phase decomposition of $WN(NMe_2)(N^iPr)_2$ (**3**).

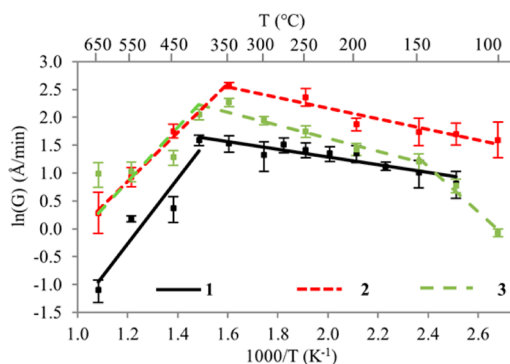


Figure 4. Growth kinetics comparing $\ln(G)$, where G is the growth rate, versus the inverse temperature for films deposited from **1–3**. The illustrated error bars are representative of thickness measurements near the center of the substrate for multiple samples and measurements.

This trend is associated commonly with parasitic reactions resulting in wall deposition upstream of the heated susceptor, premature gas-phase reactions, and/or desorption of surface-bound species. The apparent activation energies for this regime are -0.386 ± 0.008 , -0.385 ± 0.009 , and -0.200 ± 0.020 eV for **1**, **2**, and **3**, respectively. Since parasitic reactions decrease the reactant concentration available for deposition and thus the deposition rate, the reported deposition activation energies are negative. It is noted that the mass transfer to parasitic reaction controlled transition temperatures are similar for each precursor, suggesting a similar parasitic reaction. Steric control of the parasitic high-temperature process is consistent with the observed trend where the apparent activation energies for **1** and **2** are nearly identical, while that of **3** is significantly higher. The

A values for methyl and ethyl are 1.74 and 1.75, respectively, while the value for isopropyl is 2.15,³⁸ indicating a much larger steric profile for the isopropyl substituents in **3** than for the methyl and ethyl substituents in **1** and **2**.

WN_xC_y Film Composition. X-ray photoelectron spectroscopy (XPS) was used to determine the elemental composition and its atomic valence states in the films. W, N, C, and O are the only elements evident in the deposits from **3** within the detection limit of $\sim 1\%$ (Figure 5). Similar composition data for material grown from **1** and **2** were reported previously.^{31,32}

In the XPS data for deposits from **3**, the W 4f doublet peak is consistent with contributions from three separate tungsten compounds, whose nominal binding energy (BE) values³⁹ are depicted in the superimposed stick patterns. Although the WN_x and WC_{1-x} peaks are separated by approximately 0.2 eV, they are illustrated as a single WN_xC_y peak.

In the N XPS, the stick patterns are representative of nominal BEs for WN_x and CN_x at 397.5 and 400.2 eV, respectively, although they are labeled as “WN_xC_y” and “Free N” for ease of illustration. At the deposition temperature of 100 °C the primary N 1s peak contained an asymmetric tail at higher BEs that could be fitted with a peak at a BE of 400.1 eV, which is consistent with nitrogen in the form CN_x. This suggests that **3** may not fully decompose at 100 °C. At all other deposition temperatures, the only peak present was one located at 397.9 ± 0.2 eV, which is indicative of partially oxidized WN_x.

Typical BEs for C 1s peaks from WC_{1-x} reside around 283.5 eV, those for amorphous C reside between 284.5 and 285.0 eV depending on its nature, and that for CN_x lies at approximately 286.0 eV (Figure 5). In the material deposited from **3** at 100 °C, small amounts of CN_x ($\sim 11\%$) could be detected. Spectra from materials deposited at all other deposition temperatures

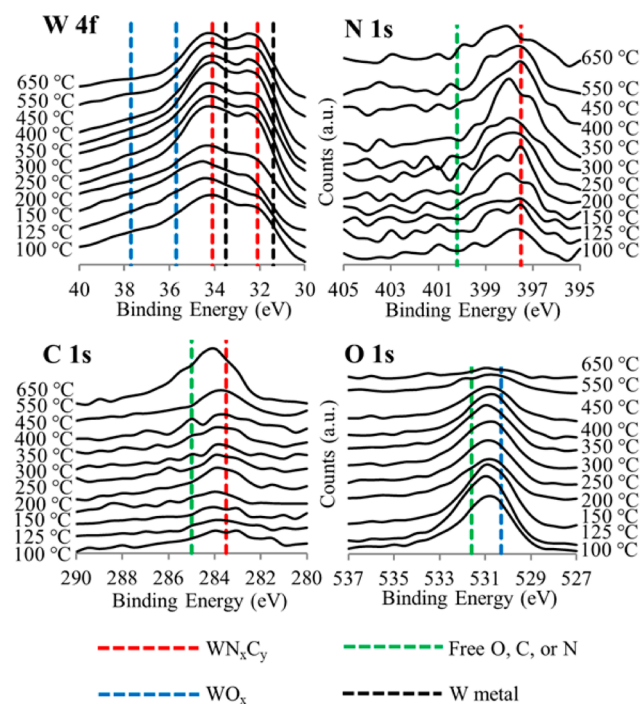


Figure 5. Evolution of the W 4f, N 1s, C 1s, and O 1s peaks with the deposition temperature using **3**. Relevant and nominal material BEs³⁹ are superimposed onto the plots by a stick pattern.

revealed only peaks corresponding to amorphous C (labeled as “Free C”) and carbidic C (i.e., C_x-W). The average amorphous C content at depositions below 300 °C was 23 ± 1%, whereas from 300 to 450 °C it was 29 ± 1%, and above 450 °C it increased to 43 ± 1% at 650 °C.

Adventitious nonstoichiometric tungsten oxide (WO_x, where 2.0 < x < 3.0) is also detected in the XPS spectrum. Although the subpeaks corresponding to WN_xC_y are relatively constant for all deposition temperatures at 32.3 ± 0.1 and 34.3 ± 0.1 eV for W 4f_{7/2} and W 4f_{5/2}, respectively, the WO_x peaks shift from 35.8 ± 0.2 and 37.6 ± 0.2 eV (below 250 °C) to 35.0 ± 0.1 and 36.7 ± 0.2 eV (at and above 250 °C) for W 4f_{7/2} and W 4f_{5/2} peaks, respectively. This suggests that higher temperature growth results in adventitious WO_x that is less fully oxidized.

Observation of WO_x in the W XPS region of films grown using **3** as a precursor can be corroborated with the O 1s peak (Figure 5). The stick patterns represent WO_x and free O, or more specifically adsorbed O₂ from the atmosphere, at 530.5 and 531.6 eV, respectively. At low deposition temperatures, the O 1s peak is an average of the two defined values, but as the deposition temperature increases, there is a slight shift in peak position toward predominantly WO_x. The average WO_x and free O peak positions are fairly constant throughout the full range of deposition temperatures with average values of 530.7 ± 0.1 and 531.9 ± 0.2 eV, respectively.

Figure 6 illustrates the percentage of nitridic N (i.e., N_x-W), oxidic O (i.e., O_x-W), and carbidic C (i.e., C_x-W), and is representative of the respective percentage occupancy of the subpeak under the primary elemental peak. Therefore, not only does the W 4f peak become less saturated with O signal with increasing deposition temperature, but the available signal is of a lower oxidation state. The elemental composition of the material deposited from **3** is plotted in Figure 7 as a function of the deposition temperature in the range from 100 to 650 °C and compared to compositions measured also by XPS for films

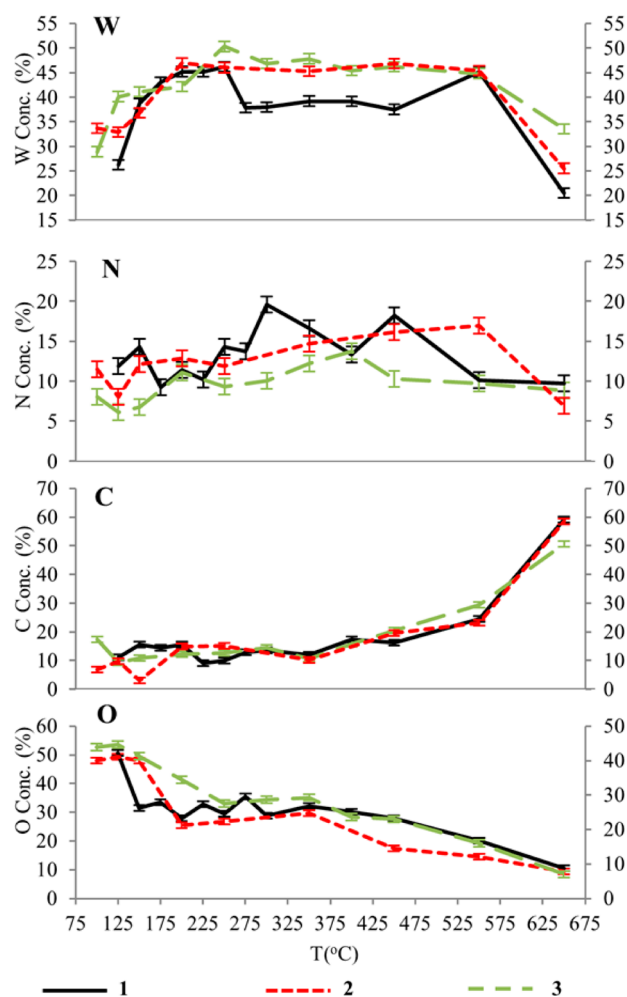


Figure 6. Influence of the precursor on the percentage of N_x-W, O_x-W, and C_x-W, according to XPS peak deconvolution.

deposited from precursors **1** and **2**. The dominant feature of this comparison is the similarity of composition variation with deposition temperature between the three precursors. This is not surprising given the similar molecular structure and apparent common rate-determining decomposition reaction. Another feature is that the W concentration is relatively constant in the middle temperature range but decreases significantly at both low and high temperature. This pattern is consistent with a trade-off for O and C incorporation at lower and higher deposition temperatures, respectively. At the low-temperature limit, **3** may undergo incomplete decomposition and adventitious O incorporation is competitive. At the high-temperature limit, premature and aggressive precursor decomposition become more significant, as does C incorporation from ligand and solvent decomposition. The N concentration using **3** is relatively constant (ranging from 6% at 100 °C to 14% at 400 °C).

Interestingly, depositions using **3** resulted in the lowest N incorporation, whereas depositions with **1** provided the most. Additionally, depositions using **1** and **3** provided almost entirely nitridic N (i.e., N_x-W), except for the two lowest deposition temperatures where there was a presence of CN_x at approximately 14% and 17%, respectively. This is unlike depositions with **2** that resulted in a minimum CN_x presence of approximately 16%, with an average of 18 ± 3% below 400 °C and 35 ± 2% above 400 °C.

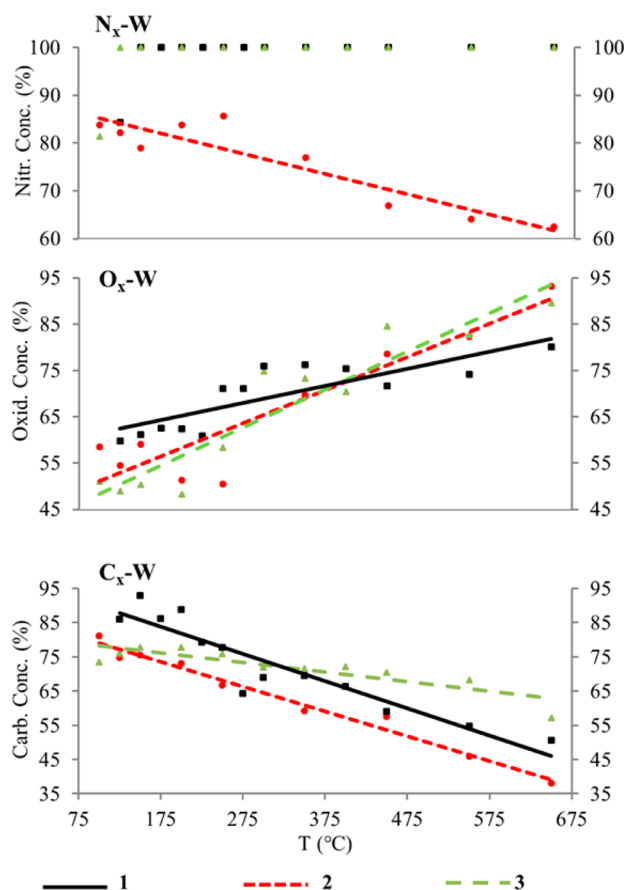


Figure 7. Elemental composition for films deposited from 1–3 at various deposition temperatures, according to XPS. Note the differences in the concentration scale.

Figure 7 further shows that C incorporation is nearly identical for all films grown from 1–3, with integration of C becoming prominent above 450 °C. This is most likely the result of solvent and/or ligand decomposition. It has been documented that pyridine undergoes surface-catalyzed decomposition at similar temperatures.^{40–43}

Figure 6 shows, however, that although qualitatively similar to depositions using 1 and 2, the extent of change in amorphous C incorporation with increasing temperature into the films was less dramatic when using 3. This result is consistent with C incorporation by ligand degradation in a surface reaction, which would be hindered by the additional steric bulk of 3.

Oxygen is incorporated into the films by two means: during film growth from adventitious O_2 and H_2O or postgrowth exposure to air. Due to the relatively low density and amorphous nature of the films, significant in-diffusion of oxygen is likely. Additionally, at these low growth temperatures, the sticking probability of gas is high, so any background O source can be integrated into the film.⁴⁴ The average percentage of WO_x below 250 °C is $51 \pm 4\%$ and increases steadily to almost 90% at 650 °C. It should be noted that although more of the incorporated O is O_x -W (Figure 6), there is less overall O content in the film (Figure 7). The decrease in postgrowth O is likely from film densification and C stuffing in the film, both of which would prevent O in-diffusion.

Deconvolution of the O 1s peaks shows that depositions from 2 and 3 experience nearly identical ratios of free O and

O_x -W, whereas films deposited from 1 experienced less O_x -W. This is the result of a density difference between the films (see Supporting Information), where films from 1 proved to be less dense.

WN_xC_y Film Microstructure. Control of the film microstructure is important in diffusion barrier applications. An amorphous barrier is preferable to a polycrystalline barrier due to the low-energy diffusion pathways that grain boundaries afford.⁴⁵ According to grazing incidence X-ray diffraction (GIXD) measurements (Figure 8), films deposited from 2

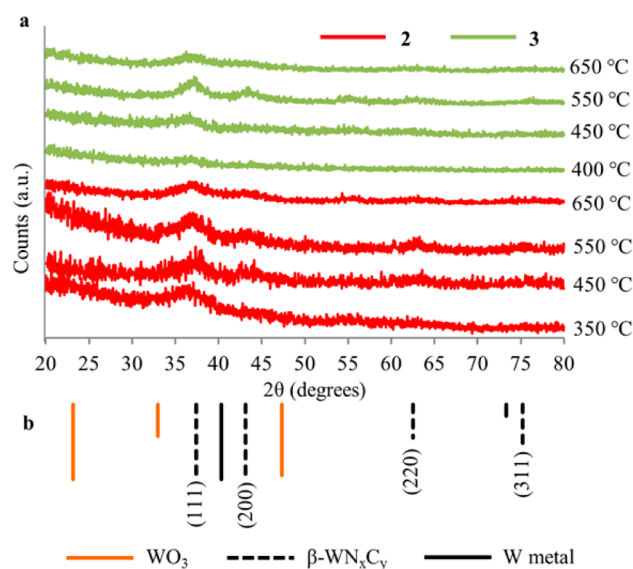


Figure 8. (a) GIXD patterns taken for films deposited using compounds 2 and 3. (b) Typical crystallographic planes for relevant materials with respect to their preferred structures and according to their relative intensities.⁴⁶

and 3 developed crystallinity at 350 and 400 °C, respectively (Figure 8b), whereas films grown from 1 were entirely amorphous for all deposition temperatures. Films deposited below 350 and 400 °C for films grown from 2 and 3, respectively, were entirely amorphous (Figure S-3). The primary β - WN_xC_y (i.e., face-centered-cubic structure) reflections are expected to result from a solid solution of β - $WN_{0.5}$ and β - $WC_{0.6}$, which have proximal reflections, and for that reason are illustrated as a single reflection. The stick pattern exists at $2\theta = 37.42^\circ$, 43.12° , 65.52° , and 75.22° for the β - WN_xC_y (111), β - WN_xC_y (200), β - WN_xC_y (220), and β - WN_xC_y (311) crystallographic planes, respectively. These powder reflections do, in fact, coincide with both β - $WN_{0.5}$ and β - $WC_{0.6}$ solutions. Similarly, the primary WO_3 stick pattern is an amalgamation of reflections for three common WO_3 phases: monoclinic, tetragonal, and cubic. There are, however, no apparent reflections for any phase of WO_3 , which should improve the barrier properties (increased structural disorder).

The peak locations of materials grown using 2 and 3 are highlighted in Table 2. In both cases there is slight preferential texturing for the β - WN_xC_y (111) plane, according to the peak prominence. Therefore, its position was used to estimate the lattice parameter, and its full width at half-maximum (fwhm) was used to estimate the lower limit of the grain size, via Scherrer's equation. The slight discrepancy in peak locations (from the standard) is expected to be from compositional variations in the film, and not lattice strain, due to the highly

Table 2. Peak Locations (2θ , deg) and fwhm Obtained by GIXD for WN_xC_y Grown with 2 and 3

growth T ($^{\circ}C$)	fwhm (111)	crystallographic planes			
		(111)	(200)	(220)	(311)
		Standard			
		37.42	43.12	65.52	75.22
		2			
350	5.13	36.77	43.42	<i>a</i>	<i>a</i>
450	3.12	37.34	43.46	63.17	<i>a</i>
550	2.91	37.38	43.45	63.06	75.58
650	3.35	37.63	43.45	63.21	75.70
		3			
400	4.71	37.01	43.83	<i>a</i>	<i>a</i>
450	3.84	36.89	43.34	62.68	<i>a</i>
550	3.02	37.26	43.45	62.91	75.95
650	3.23	37.38	43.45	62.81	<i>a</i>

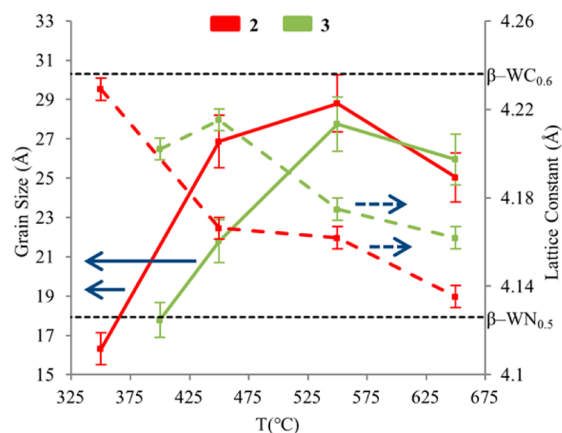
^aNot available.

disordered nature of the film as evident in the nanocrystalline domain sizes described in the next section.

Recall that the XPS data indicate that W is bound to C, N, and O. From that analysis it is expected that those components belong to a fully integrated $WN_xC_yO_z$ matrix, separate interspersed matrixes such as WN_x , WC_x , and WO_x or any permutation in between (e.g., WN_xC_y and WO_x ; WN_xO_y and WC_x ; WN_x and WC_xO_y). The crystallographic data obtained using GIXD (Figure 8) suggest that WN_x , WC_x , or the solid solution WN_xC_y phases exist and adopt a face-centered-cubic structure. Unfortunately, it cannot be stated with confidence that a separate and distinct WO_x phase exists. The data are consistent with formation of a crystalline β - WN_xC_y core phase surrounded by $WN_xC_yO_z$ solid solution, which forms upon air exposure. Therefore, the lattice parameter of that crystalline phase should lie around the values of β - WN_x or β - WC_x . The lattice constants for β - $WC_{0.6}$ and β - $WN_{0.5}$ are 4.236 and 4.126 Å, respectively. The lattice parameters for crystalline films grown with 2 and 3 decrease with increasing deposition temperature and have maximum values of 4.229 and 4.215 Å and minimum values of 4.135 and 4.162 Å, respectively. It is expected that β - WN_xC_y would produce lattice parameter values between the end points of the solid solution tie line.

The trend seen in Figure 9 is consistent with the valence-state information obtained through XPS. It has been shown that lattice constants can increase with deposition temperature as a result of greater incorporation of C into the lattice.¹⁵ Films deposited from 2 and 3 do in fact contain greater C levels at higher deposition temperatures; however, it is important to note that the percentage of C_x -W decreases with increasing temperature. Consequently, a decrease in the lattice constant with respect to the β - $WC_{0.6}$ lattice constant is seen for films grown from both 2 and 3. This is especially true for films grown with 2, where amorphous C becomes more fully integrated.

Average N values remain relatively constant, which pulls the lattice parameter closer to the standard β - $WN_{0.5}$ value. Films deposited with 2, however, initially crystallize with a larger lattice constant than those from 3, a difference that can be attributed to CN_x , the incidental N species. Below 400 °C in films grown from 2, 75% of the N signal is nitridic (i.e., N_x -W), which can yield a comparatively greater lattice parameter due to the preoccupation of N in the film. Films grown with 3 at 400 °C do not contain CN_x species, so the lattice constant favors 4.126 Å. For films grown from 2, a sharp descent toward the β -

**Figure 9.** Illustration of the deposition temperature dependence of the crystal grain size (left vertical axis) and crystal lattice parameter (right vertical axis). The standard crystal lattice constants for β - $WN_{0.5}$ (4.126 Å) and β - $WC_{0.6}$ (4.236 Å) are imposed on the plot for reference.

$WN_{0.5}$ standard peak position for the film grown at 450 °C is due to increasing amorphous C and CN_x concentrations, where N exists nearly equally in its two environments. This produces interstitial vacancies that contract the lattice. Conversely, films grown from 3 do not produce such an exaggerated decrease in lattice parameter due to greater concentrations of nitridic and carbidic N and C, respectively.

It should be noted that although there was no indication of a crystalline WO_x phase, O could influence the estimated lattice parameters. It is assumed, however, that O exists exclusively in the amorphous WN_xC_y matrix that envelops the β - WN_xC_y nanodomains, given its likely atmospheric origin, and therefore, any influence it has on the lattice parameters has been discounted.

On average, material grown with 2 is similar in estimated grain size to that grown with 3. The estimated minimum grain sizes are 16.3 and 17.8 Å, respectively, and the maximum estimated grain sizes are 28.8 and 27.8 Å, respectively (Figure 9). The grain sizes obtained from both precursors increase with deposition temperatures up to 550 °C. This is likely a result of increased surface and bulk mobility with increasing deposition temperature, which promotes grain growth. At 650 °C, the grain size decreases slightly to 25.0 and 26.0 Å for films deposited from 2 and 3, respectively. Despite the enhanced mobility of surface species at this temperature, it is likely that the increasing amounts of adventitious C begin to interfere with the crystallization process at high temperatures.^{47,48} This effect is greater for films grown with 2 where there is more adventitious C present.

Diffusion Barrier Testing. The tests of films grown from 1 and 2 as Cu diffusion barriers have been presented elsewhere.^{31,32} The integrity of the film grown from 3 as a diffusion barrier is discussed here. Thin WN_xC_y films (~5 nm thickness) grown from 3 at 150 °C were evaluated by depositing approximately 100 nm of Cu onto a WN_xC_y film and annealing the Cu/ WN_xC_y /Si stack at 500 °C for 30 min under N_2 .

An etch-pit test was performed to evaluate Cu diffusion through the barrier. The etch-pit test has greater sensitivity to Cu diffusion than either four-point probe (4PP) or XRD measurements (Figure S-2). Figure 10 displays scanning electron microscopy (SEM) plane-view images of etched films on the postannealed Cu/ WN_xC_y /Si stacks (Figure 10a,b), the as-deposited Cu/ WN_xC_y /Si stacks (Figure 10c),

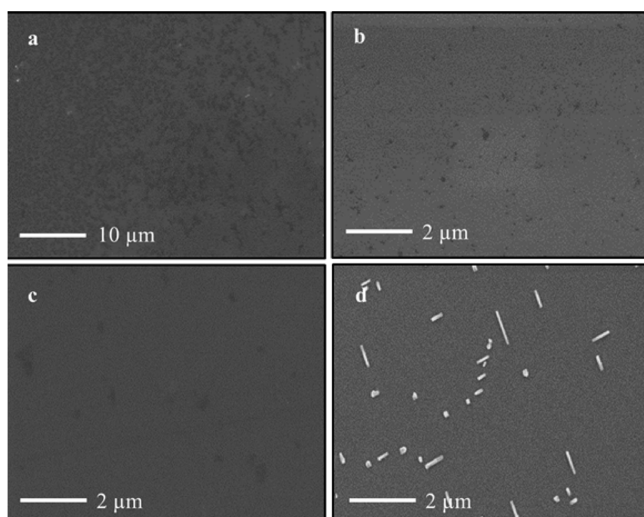


Figure 10. (a) Plane-view image of the etch-pit test for the postannealed Cu/WN_xC_y/Si stack at lower magnification, (b) plane-view image of the etch-pit test for the postannealed Cu/WN_xC_y/Si stack at higher magnification, (c) plane-view image of the etch-pit test for the as-deposited Cu/WN_xC_y/Si stack, and (d) image of a failed postannealed Cu/WN_xC_y/Si stack for comparison purposes.

and a failed barrier for comparison (Figure 10d). In the event of even small-scale Cu diffusion to the surface, micrometer-sized inverted pyramidal features (appearing as bright rectangles in Figure 10d) would be visible on the surfaces. The lack of inverted pyramidal features in parts a (lower magnification) and b (higher magnification) of Figure 10 is evidence for successful barrier performance by films deposited from 3.

An additional test for barrier evaluation was to examine the interfaces with high-resolution transmission electron microscopy (HRTEM). Figure 11 is a cross-sectional HRTEM image depicting the well-defined interfaces present in a postannealed Cu/WN_xC_y/Si sample. The single-crystal lattice structures of the Si substrate and the polycrystalline Cu film are clearly visible. The amorphous nature of the native silicon oxide (SiO₂) and WN_xC_y films is also evident.

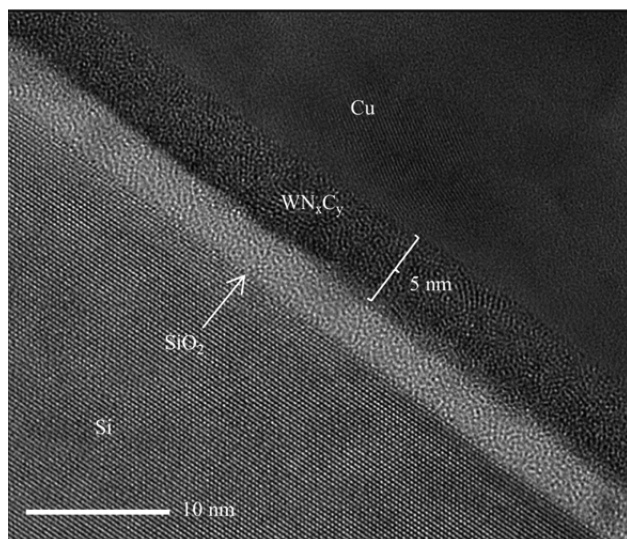


Figure 11. HRTEM image clearly showing smooth and distinct boundaries for a postannealed Cu/WN_xC_y/Si sample grown from 3.

CONCLUSION

By manipulation of reaction conditions, several compounds of the type WN(NR₂)₃ were synthesized. Reduced symmetry and increased steric bulk were associated with improved volatility, an important property for use of the compounds in conventional CVD or ALD. The TGA of 3 was characteristic of sublimation. We have successfully deposited WN_xC_y thin films at temperatures as low as 100 °C by using AACVD from pyridine solutions of 3 (0.051 M). The effect of the ligand structure on the film properties has been ascertained. It was determined that 2 and 3 offer more desirable film properties for diffusion barrier applications in terms of growth rate, surface roughness, composition, and density. The integrity of thin films deposited from 3 was evaluated for inhibition of Cu diffusion by 4PP, XRD, SEM etch-pit test, and HRTEM measurements. Cu (~100 nm)/WN_xC_y (~5 nm)/Si stacks successfully passed annealing at 500 °C for 30 min in N₂. Therefore, 3 was identified as a viable single-source precursor for deposition of WN_xC_y for Cu diffusion barrier applications.

EXPERIMENTAL SECTION

General Procedures. Unless otherwise specified, all manipulations were performed under an inert atmosphere (N₂, Ar) using standard Schlenk and glovebox techniques. Toluene was purified using an MBraun MB-SP solvent purification system and stored over activated 3 Å molecular sieves prior to use. Benzene-*d*₆ was purchased from Cambridge Isotope Laboratories, Inc. and stored over activated 3 Å molecular sieves (15%, w/v) for several days in an inert atmosphere glovebox prior to use. Anhydrous *tert*-butyl alcohol, pentane, and redistilled diisopropylamine were purchased from Sigma-Aldrich and used as received. Hexamethyldisiloxane and pyridine were purchased from Sigma-Aldrich or Alfa Aesar and stored over activated 3 Å molecular sieves (15%, w/v) for several days in an inert atmosphere glovebox prior to use. Compounds 1–4 and 19–20 were prepared as previously described.^{30,31} All other chemicals were purchased and used as received. ¹H and ¹³C NMR spectra were obtained using Gemini, Mercury, or VXR 300 MHz spectrometers (Varian shims/probes, Oxford magnets) using the residual protons of the deuterated solvents as reference peaks. Mass spectra were obtained with a Thermo Scientific Trace GC DSQ mass spectrometer using the direct inlet probe chemical ionization (DIP-CI) mode of operation or an Agilent 6200 ESI-TOF mass spectrometer using the direct analysis in real time time-of-flight (DART-TOF) mode of operation.

General Synthesis Procedure A. In a 100 mL Schlenk flask, 0.25 g (0.76 mmol) of 1 and 60 mL of pentane were combined to create a white slurry. To the slurry was added the amine in excess to give an orange-red suspension. A reflux condenser was attached, and the mixture was brought to a gentle reflux under argon. After 12 h, the resulting amber-brown solution was returned to room temperature, and the solvent was removed under vacuum. The product was extracted by stirring with hexamethyldisiloxane (30 mL) for 15 min and filtered through Celite. The filter pad was washed with additional hexamethyldisiloxane (2 × 5 mL). The solvent was removed from the filtrate to give a crude solid. Sublimation of the crude product gave pure product.

WN(NMe₂)(*n*Bu)₂ (5). Compound 5 was synthesized by general synthesis procedure A. The crude product was purified by sublimation at 150–250 mTorr and 80–85 °C to afford an orange-white solid. Yield: 60%. ¹H NMR (C₆D₆, 300 MHz): δ 0.95 [dd, *J* = 6.3 Hz, 24H, –N(CH₂H_bCH(CH₃)_c(CH₃)_d)]; 1.98 [sp, *J* = 7 Hz, 4H, –N(CH₂H_bCH(CH₃)_c(CH₃)_d)]; 3.40 [s, 6H, –N(CH₃)₂]; 3.49 [d, *J* = 6 Hz, 4H, –N(CH₂H_bCH(CH₃)_c(CH₃)_d)]; 3.55 [d, *J* = 6.6 Hz, 4H, –N(CH₂H_bCH(CH₃)_c(CH₃)_d)]. ¹³C NMR (C₆D₆, 300 MHz): δ 20.4 [–N(CH₂H_bCH(CH₃)_c(CH₃)_d)]; 20.7 [–N(CH₂H_bCH(CH₃)_c(CH₃)_d)]; 27.1 [–N(CH₂H_bCH(CH₃)_c(CH₃)_d)]; 52.4 [–N(CH₃)₂]; 66.5 [–N(CH₂H_bCH(CH₃)_c(CH₃)_d)]. DIP-CI-MS: calcd for [M + H]⁺ 497.2970; found 497.2950.

$WN(N(CH_2)_5)_3$ (**6**). Compound **6** was synthesized by general synthesis procedure A. The crude product was purified by sublimation at 150–250 mTorr and 70–80 °C to afford an orange solid. Yield: 60%. 1H NMR (C_6D_6 , 300 MHz): δ 1.39 [m, 6H, $-NCH_2CH_2CH_2$]; 1.47 [m, 12H, $-NCH_2CH_2CH_2$]; 3.80 [t, $J = 6$ Hz, 12H, $-NCH_2CH_2CH_2$]. ^{13}C NMR (C_6D_6 , 300 MHz): δ 25.2 [$-N(CH_2CH_2CH_2)$]; 29.7 [$-N(CH_2CH_2CH_2)$]; 60.7 [$-N(CH_2CH_2CH_2)$]. DIP-Cl-MS: calcd for $[M + H]^+$ 449.2931; found 449.2934.

$WN(N(CH_2)_6)_3$ (**7**). Compound **7** was synthesized by general synthesis procedure A. The crude product was purified by sublimation at 150–250 mTorr and 75–85 °C to afford an orange solid. Yield: 55%. 1H NMR (C_6D_6 , 300 MHz): δ 1.51 [br m, 6H, $-NCH_2CH_2CH_2$]; 1.75 [br m, 12H, $-NCH_2CH_2CH_2$]; 3.80 [t, $J = 6$ Hz, 12H, $-NCH_2CH_2CH_2$]. ^{13}C NMR (C_6D_6 , 300 MHz): δ 26.8 [$-N(CH_2CH_2CH_2)$]; 33.6 [$-N(CH_2CH_2CH_2)$]; 61.3 [$-N(CH_2CH_2CH_2)$]. DIP-Cl-MS: calcd for $[M + H]^+$ 493.2525; found 493.2513.

General Synthesis Procedure B. In a 200 mL Schlenk flask, 0.50 g (1.5 mmol) of **1** and 80 mL of pentane were combined to form a white slurry. To the slurry was added 6.0 mL of diisopropylamine (4.3 g, 43 mmol) to give an orange-red suspension. A reflux condenser was attached, and the mixture was brought to a gentle reflux under Ar. After 12 h, the solvent was removed from the amber-brown solution under vacuum at room temperature. The residue was extracted by stirring with hexamethyldisiloxane (50 mL) for 15 min and filtered through Celite. The filter pad was washed with additional hexamethyldisiloxane (2×5 mL). The solvent was removed from the resulting brown filtrate under vacuum to give crude **4**. This was dissolved in pentane (60 mL), and amine was added in excess. A reflux condenser was attached, and the mixture was brought to a gentle reflux under Ar. After 12 h, the solvent was removed from the dark brown solution under vacuum at room temperature. Sublimation of the crude residue afforded pure product.

$WN(N(CH_2)_5)_2(N^iPr)_2$ (**8**). Compound **8** was synthesized by general synthesis procedure B. The crude product was purified by sublimation at 15–250 mTorr and 60–70 °C to afford an orange-white solid. Yield: 50%. 1H NMR (C_6D_6 , 300 MHz): δ 1.30 [br m, 8H, $-NCH_2CH_2CH_2$]; 1.40 [d, $J = 3$ Hz, 12H, $-N(CH(CH_3)_2)_2$]; 1.47 [br m, 4H, $-NCH_2CH_2CH_2$]; 3.44 [m, 2H, $-N(CH(CH_3)_2)_2$]; 3.80 [t, $J = 6$ Hz, 12H, $-NCH_2CH_2CH_2$]. ^{13}C NMR (C_6D_6 , 300 MHz): δ 25.2 [$-N(CH(CH_3)_2)_2$]; 26.4 [$-NCH_2CH_2CH_2$]; 29.7 [$-NCH_2CH_2CH_2$]; 51.0 [$-N(CH(CH_3)_2)_2$]; 60.7 [$-NCH_2CH_2CH_2$]. MS (DART-TOF): calcd for $[M + H]^+$ 467.2368; found 467.2346.

$WN(N(CH_2)_6)_2(N^iPr)_2$ (**9**). Compound **9** was synthesized by general synthesis procedure B. The crude product was purified by sublimation at 15–250 mTorr and 70–80 °C to afford an orange-white solid. Yield: 50%. 1H NMR (C_6D_6 , 300 MHz): δ 1.36 [dd, $J = 24, 6$ Hz, 12H, $-N(CH(CH_3)_2)_2$]; 1.52 [br m, 8H, $-NCH_2CH_2CH_2$]; 1.78 [br m, 4H, $-NCH_2CH_2CH_2$]; 3.47 [m, $J = 6$ Hz, 2H, $-N(CH(CH_3)_2)_2$]; 3.81 [t, $J = 6$ Hz, 12H, $-NCH_2CH_2CH_2$]. ^{13}C NMR (C_6D_6 , 300 MHz): δ 26.4 [$-N(CH(CH_3)_2)_2$]; 26.8 [$-NCH_2CH_2CH_2$]; 33.5 [$-NCH_2CH_2CH_2$]; 50.9 [$-N(CH(CH_3)_2)_2$]; 61.6 [$-NCH_2CH_2CH_2$]. MS (DART-TOF): calcd for $[M + H]^+$ 495.2681; found 495.2694.

$WN(N^iPr)_2(N^iPr)_2$ (**10**). Compound **10** was synthesized by general synthesis procedure B. The crude product was purified by sublimation at 150–250 mTorr and 65–75 °C to afford an orange-white solid. Yield: 50%. 1H NMR (C_6D_6 , 300 MHz): δ 0.87 [t, $J = 7$ Hz, 12H, $-N(CH_2CH_2CH_3)$]; 1.36 [d, $J = 6$ Hz, 12H, $-N(CH(CH_3)_2)_2$]; 1.64 [sp, $J = 7$ Hz, 8H, $-N(CH_2CH_2CH_3)_2$]; 3.42 [sp, 2H, $-N(CH(CH_3)_2)_2$]; 3.56–3.68 [m, 8H, $-N(CH_2CH_2CH_3)_2$]. ^{13}C NMR (C_6D_6 , 300 MHz): δ 12.1 [$-N(CH(CH_3)_2)_2$]; 25.1 [$-N(CH_2CH_2CH_3)_2$]; 26.6 [$-N(CH_2CH_2CH_3)_2$]; 51.4 [$-N(CH(CH_3)_2)_2$]; 61.4 [$-N(CH_2CH_2CH_3)_2$]. MS (DART-TOF): calcd for $[M + H]^+$ 499.2994; found 499.2993.

General Synthesis Procedure C. In a 100 mL Schlenk flask, 0.50 g (1.5 mmol) of **1** and 10 mL of diisopropylamine (7.2 g, 71 mmol) were combined to create an orange-red suspension. A reflux condenser was attached, and the mixture was brought to a gentle reflux under Ar. After 12 h, the solvent was removed from the dark brown solution under vacuum at room temperature. The residue was extracted by

stirring with hexamethyldisiloxane (50 mL) for 15 min and filtered through Celite. The filter pad was washed with additional hexamethyldisiloxane (2×5 mL). The solvent was removed from the resulting brown filtrate under vacuum to give crude **3**, which was slurried in excess amine. A reflux condenser was attached, and the mixture was brought to a gentle reflux under Ar. After 6 h, the solvent was removed from the dark brown solution under vacuum at room temperature. Sublimation of the crude residue afforded pure product.

$WN(N(CH_2)_5)_2(N^iPr)_2$ (**11**). Compound **11** was synthesized by general synthesis procedure C. The crude product was purified by sublimation at 150–250 mTorr and 55–65 °C to afford an orange-white solid. Yield: 50%. 1H NMR (C_6D_6 , 300 MHz): δ 1.30 [d, $J = 6$ Hz, 12H, $-N(CH(CH_3)_a(CH_3)_b)$]; 1.39 [d, $J = 6$ Hz, 12H, $-N(CH(CH_3)_a(CH_3)_b)$]; 1.44–1.49 [m, 6H, $-NCH_2CH_2CH_2$]; 3.44 [m, $J = 6$ Hz, 4H, $-N(CH(CH_3)_a(CH_3)_b)$]; 3.80 [t, $J = 6$ Hz, 4H, $-NCH_2CH_2CH_2$]. ^{13}C NMR (C_6D_6 , 300 MHz): δ 25.2 [$-N(CH(CH_3)_a(CH_3)_b)$]; 25.9 [$-N(CH(CH_3)_a(CH_3)_b)$]; 26.6 [$-NCH_2CH_2CH_2$]; 29.3 [$-NCH_2CH_2CH_2$]; 51.2 [$-N(CH(CH_3)_a(CH_3)_b)$]; 61.6 [$-NCH_2CH_2CH_2$]. MS (DART-TOF): calcd for $[M + H]^+$ 483.2681; found 483.2663.

$WN(N(CH_2)_6)_2(N^iPr)_2$ (**12**). Compound **12** was synthesized by general synthesis procedure C. The crude product was purified by sublimation at 150–250 mTorr and 60–65 °C to afford an orange-white solid. Yield: 50%. 1H NMR (C_6D_6 , 300 MHz): δ 1.31 [d, $J = 6$ Hz, 12H, $-N(CH(CH_3)_a(CH_3)_b)$]; 1.39 [d, $J = 6$ Hz, 12H, $-N(CH(CH_3)_a(CH_3)_b)$]; 1.52 [br m, 6H, $-NCH_2CH_2CH_2$]; 1.78 [br m, 6H, $-NCH_2CH_2CH_2$]; 3.47 [sp, $J = 6$ Hz, 4H, $-N(CH(CH_3)_a(CH_3)_b)$]; 3.80 [t, $J = 6$ Hz, 4H, $-NCH_2CH_2CH_2$]. ^{13}C NMR (C_6D_6 , 300 MHz): δ 25.3 [$-N(CH(CH_3)_a(CH_3)_b)$]; 26.4 [$-NCH(CH_3)_a(CH_3)_b$]; 26.8 [$-NCH_2CH_2CH_2$]; 33.2 [$-NCH_2CH_2CH_2$]; 51.1 [$-NCH(CH_3)_a(CH_3)_b$]; 61.6 [$-NCH_2CH_2CH_2$]. MS (DART-TOF): calcd for $[M + H]^+$ 497.2838; found 497.2861.

$WN(N^iPr)_2(N^iPr)_2$ (**13**). Compound **13** was synthesized by general synthesis procedure C. The crude product was purified by sublimation at 200–300 mTorr and 50–55 °C to afford an orange-white solid. Yield: 35%. 1H NMR (C_6D_6 , 300 MHz): δ 0.85 [t, $J = 6$ Hz, 6H, $-N(CH_2CH_2CH_3)_2$]; 0.87 [t, $J = 6$ Hz, 6H, $-N(CH_2CH_2CH_3)_2$]; 1.30 [d, $J = 6$ Hz, 12H, $-N(CH(CH_3)_2)_2$]; 1.37 [d, $J = 6$ Hz, 12H, $-N(CH(CH_3)_2)_2$]; 1.62 [sextet, $J = 6$ Hz, 4H, $-N(CH_2CH_2CH_3)_2$]; 3.52 [sp, $J = 6$ Hz, 4H, $-N(CH(CH_3)_2)_2$]; 3.60 [t, $J = 6$ Hz, 4H, $-N(CH_2CH_2CH_3)_2$]. ^{13}C NMR (C_6D_6 , 300 MHz): δ 12.11 [$-N(CH_2CH_2CH_3)_2$]; 12.25 [$-N(CH_2CH_2CH_3)_2$]; 25.21 [$-N(CH_2CH_2CH_3)_2$]; 25.26 [$-N(CH_2CH_2CH_3)_2$]; 26.43 [$-N(CH(CH_3)_2)_2$]; 26.73 [$-N(CH(CH_3)_2)_2$]; 51.64 [$-N(CH_2CH_2CH_3)_2$]; 61.60 [$-N(CH(CH_3)_2)_2$]. MS (DART-TOF): calcd for $[M + H]^+$ 499.2994; found 499.2996.

General Synthesis Procedure D. In a 200 mL Schlenk flask, 0.50 g (1.3 mmol) of **4** and 80 mL of pentane were combined to form a white slurry. To the slurry was added 8.0 mL of diisobutylamine (5.9 g, 46 mmol) to give an orange-red suspension. A reflux condenser was attached, and the mixture was brought to a gentle reflux under Ar. After 12 h, the solvent was removed from the amber-brown solution under vacuum at room temperature. The residue was extracted by stirring with hexamethyldisiloxane (50 mL) for 15 min and filtered through Celite. The filter pad was washed with additional hexamethyldisiloxane (2×5 mL). The solvent was removed from the resulting brown filtrate under vacuum to give the crude product. This was dissolved in pentane (60 mL), and the amine was added in excess. A reflux condenser was attached, and the mixture was brought to a gentle reflux under Ar. After 3 h, the solvent was removed from the dark brown solution under vacuum at room temperature. Sublimation of the crude residue afforded pure product.

$WN(NMe_2)(N^iPr)_2(N^iBu)_2$ (**16**). Compound **16** was synthesized by general synthesis procedure D. The crude product was purified by sublimation at 150–250 mTorr and 45–55 °C to afford an orange-white solid. Yield: 50%. 1H NMR (C_6D_6 , 300 MHz): δ 0.91 [d, $J = 6$ Hz, 6H, $-NCH_2CH(CH_3)_a(CH_3)_b$]; 0.99 [d, $J = 6$ Hz, 6H, $-NCH_2CH(CH_3)_a(CH_3)_b$]; 1.28 [d, $J = 6$ Hz, 12H, $-N(CH(CH_3)_a(CH_3)_b)$]; 1.36 [d, $J = 6$ Hz, 12H, $-N(CH(CH_3)_a(CH_3)_b)$]; 1.97 [sp, $J = 6$ Hz, 2H, $-NCH_2CH(CH_3)_a(CH_3)_b$]; 3.37 [s, 6H, $-N(CH_3)_2$];

3.43–3.54 [m, $J = 6$ Hz, 12H, $-N(CH(CH_3)_a(CH_3)_b)$, $-NCH_2CH(CH_3)_a(CH_3)_b$]; ^{13}C NMR (C_6D_6 , 300 MHz): δ 20.1 [$-NCH_2CH(CH_3)_a(CH_3)_b$]; 20.8 [$-NCH_2CH(CH_3)_a(CH_3)_b$]; 25.8 [$-N(CH(CH_3)_a(CH_3)_b)$]; 26.7 [$-N(CH(CH_3)_a(CH_3)_b)$]; 27.2 [$-NCH_2CH(CH_3)_a(CH_3)_b$]; 51.0 [$-N(CH_3)_2$]; 51.9 [$-N(CH(CH_3)_a(CH_3)_b)$]; 66.2 [$-NCH_2CH(CH_3)_a(CH_3)_b$]. DIP-Cl-MS: calcd for $[M + H]^+$ 471.2681; found 471.2690

WN(NEt)₂(NⁱPr)₂(NⁱBu)₂ (17). Compound 17 was synthesized by general synthesis procedure D. The crude product was purified by sublimation at 150–250 mTorr and 40–50 °C to afford an orange-white solid. Yield: 45%. 1H NMR (C_6D_6 , 300 MHz): δ 0.94 [d, $J = 6$ Hz, 6H, $-NCH_2CH(CH_3)_a(CH_3)_b$]; 0.95 [d, $J = 6$ Hz, 6H, $-NCH_2CH(CH_3)_a(CH_3)_b$]; 1.15 [t, $J = 6$ Hz, 3H, $-N(CH_2CH_3)_a(CH_2CH_3)_b$]; 1.17 [t, $J = 6$ Hz, 3H, $-N(CH_2CH_3)_a(CH_2CH_3)_b$]; 1.31 [d, $J = 6$ Hz, 6H, $-N(CH(CH_3)_a(CH_3)_b)$]; 1.36 [d, $J = 6$ Hz, 6H, $-N(CH(CH_3)_a(CH_3)_b)$]; 1.97 [sp, $J = 6$ Hz, 2H, $-NCH_2CH(CH_3)_a(CH_3)_b$]; 3.37–3.67 [m, 10H, $-NCH_2CH_2$, $-N(CH(CH_3)_a(CH_3)_b)$, $-NCH_2CH(CH_3)_a(CH_3)_b$]. ^{13}C NMR (C_6D_6 , 300 MHz): δ 16.5 [$-N(CH_2(CH_3)_a(CH_2(CH_3)_b))$]; 16.8 [$-N(CH_2(CH_3)_a(CH_2(CH_3)_b))$]; 20.1 [$-NCH_2CH(CH_3)_a(CH_3)_b$]; 20.4 [$-NCH_2CH(CH_3)_a(CH_3)_b$]; 25.8 [$-N(CH(CH_3)_a(CH_3)_b)$]; 26.3 [$-N(CH(CH_3)_a(CH_3)_b)$]; 27.1 [$-NCH_2CH(CH_3)_a(CH_3)_b$]; 50.6 [$-N(CH_2(CH_3)_a(CH_2(CH_3)_b))$]; 52.0 [$-N(CH(CH_3)_a(CH_3)_b)$]; 66.2 [$-NCH_2CH(CH_3)_a(CH_3)_b$]. DIP-Cl-MS: calcd for $[M + H]^+$ 499.2994; found 499.2998.

WN(N(CH₂)₅(NⁱPr)₂(NⁱBu)₂ (18). Compound 18 was synthesized by general synthesis procedure D. The crude product was purified by sublimation at 150–250 mTorr and 42–50 °C to afford an orange-white solid. Yield: 45%. 1H NMR (C_6D_6 , 300 MHz): δ 1.00 [d, $J = 6$ Hz, 12H, $-NCH_2CH(CH_3)_2$]; 1.29–1.46 [m, 18H, $-N(CH(CH_3)_a(CH_3)_b)$, $-NCH_2CH_2CH_2$]; 1.98 [sp, $J = 6$ Hz, 2H, $-NCH_2CH(CH_3)_2$]; 3.44 [m, $J = 6$ Hz, 2H, $-N(CH(CH_3)_a(CH_3)_b)$]; 3.62 [br m, 4H, $-NCH_2CH(CH_3)_a(CH_3)_b$]; 3.80 [t, $J = 6$ Hz, 4H, $-NCH_2CH_2CH_2$]. ^{13}C NMR (C_6D_6 , 300 MHz): δ 20.4 [$-NCH_2CH(CH_3)_a(CH_3)_b$]; 20.8 [$-NCH_2CH(CH_3)_a(CH_3)_b$]; 25.0 [$-N(CH(CH_3)_a(CH_3)_b)$]; 25.2 [$-N(CH(CH_3)_a(CH_3)_b)$]; 27.2 [$-NCH_2CH(CH_3)_a(CH_3)_b$]; 27.4 [$-NCH_2CH_2CH_2$]; 33.5 [$-NCH_2CH_2CH_2$]; 51.1 [$-N(CH(CH_3)_a(CH_3)_b)$]; 60.7 [$-NCH_2CH_2CH_2$]; 66.5 [$-NCH_2CH(CH_3)_a(CH_3)_b$]. MS (DART-TOF): calcd for $[M + H]^+$ 511.2995; found 511.2995.

WN(N(CH₂)₆(NⁱPr)₂(NⁱBu)₂ (19). Compound 19 was synthesized by general synthesis procedure D. The crude product was purified by sublimation at 150–250 mTorr and 42–50 °C to afford an orange-white solid. Yield: 45%. 1H NMR (C_6D_6 , 300 MHz): δ 0.89 [d, $J = 6$ Hz, 6H, $-NCH_2CH(CH_3)_a(CH_3)_b$]; 0.98 [d, $J = 6$ Hz, 6H, $-NCH_2CH(CH_3)_a(CH_3)_b$]; 1.30–1.38 [d, $J = 6$ Hz, 12H, $-N(CH(CH_3)_a(CH_3)_b)$]; 1.52 [br m, 6H, $-NCH_2CH_2CH_2$]; 1.78 [br m, 6H, $-NCH_2CH_2CH_2$]; 1.99 [sp, $J = 6$ Hz, 2H, $-NCH_2CH(CH_3)_a(CH_3)_b$]; 3.47 [m, 2H, $-N(CH(CH_3)_a(CH_3)_b)$]; 3.60 [br m, 4H, $-NCH_2CH(CH_3)_a(CH_3)_b$]; 3.81 [t, $J = 6$ Hz, 4H, $-NCH_2CH_2CH_2$]. ^{13}C NMR (C_6D_6 , 300 MHz): δ 20.3 [$-NCH_2CH(CH_3)_a(CH_3)_b$]; 20.8 [$-NCH_2CH(CH_3)_a(CH_3)_b$]; 26.4 [$-N(CH(CH_3)_a(CH_3)_b)$]; 26.8 [$-N(CH(CH_3)_a(CH_3)_b)$]; 26.9 [$-NCH_2CH_2CH_2$]; 27.3 [$-NCH_2CH(CH_3)_a(CH_3)_b$]; 33.5 [$-NCH_2CH_2CH_2$]; 51.1 [$-N(CH(CH_3)_a(CH_3)_b)$]; 61.6 [$-NCH_2CH_2CH_2$]; 66.4 [$-NCH_2CH(CH_3)_a(CH_3)_b$]. DIP-Cl-MS: calcd for $[M + H]^+$ 523.3126; found 523.3127.

WN_xC_y Deposition. Pure solid 1, 2, and 3 were separately dissolved in pyridine at a concentration of 0.051 M and independently deposited according to methods reported elsewhere.^{31,32}

Diffusion Barrier Testing. The procedure for diffusion barrier testing has been published elsewhere.³²

■ ASSOCIATED CONTENT

Supporting Information

The Supporting Information is available free of charge on the ACS Publications website at DOI: 10.1021/acs.chemmater.5b03691.

1H NMR spectra of compounds 5–13 and 16–19, experimental procedures for DFT calculations, thermolysis of 3 and diffusion barrier testing, 4PP measurements and XRD results for diffusion barrier tests, film surface roughness and density measurements of films grown from 3, TGA of 3 and 4, Cartesian coordinates for species on the calculated pathways for decomposition of 2 and 3, and selected m/z values from the mass spectra of compounds 5–13 and 16–19 (PDF)

■ AUTHOR INFORMATION

Corresponding Author

*E-mail: lmwhite@chem.ufl.edu.

Author Contributions

||A.K. and C.T.O. contributed equally to this work.

Notes

The authors declare no competing financial interest.

■ ACKNOWLEDGMENTS

We thank the National Science Foundation for support under NSF Grant CHE-0911640. We thank Hankook Kim for assistance with collecting the GIXD data. We thank the Major Analytical Instrumentation Center of the Engineering Department at the University of Florida for providing and maintaining the materials characterization equipment.

■ REFERENCES

- Istratov, A.; Weber, E. Physics of copper in silicon. *J. Electrochem. Soc.* **2002**, *149*, G21–G30.
- International Technology Roadmap for Semiconductors (IRTS), 2013.
- Kaloyeros, A. E.; Chen, X. M.; Stark, T.; Kumar, K.; Seo, S.; Peterson, G. G.; Frisch, H. L.; Arkles, B.; Sullivan, J. Tantalum nitride films grown by inorganic low temperature thermal chemical vapor deposition - Diffusion barrier properties in copper metallization. *J. Electrochem. Soc.* **1999**, *146*, 170–176.
- Srinivasan, N. B.; Thiede, T. B.; de los Arcos, T.; Gwildies, V.; Krasnopolski, M.; Becker, H. W.; Rogalla, D.; Devi, A.; Fischer, R. A. Transition metal nitride thin films grown by MOCVD using amidinato based complexes $[M(NtBu)_2\{(iPrN)_2CMe\}_2]$ ($M = Mo, W$) as precursors. *Surf. Coat. Technol.* **2013**, *230*, 130–136.
- Fix, R.; Gordon, R. G.; Hoffman, D. M. Chemical-Vapor Deposition of Vanadium, Niobium, and Tantalum Nitride Thin-Films. *Chem. Mater.* **1993**, *5*, 614–619.
- Kaloyeros, A.; Eisenbraun, E. Ultrathin diffusion barriers/liners for gigascale copper metallization. *Annu. Rev. Mater. Sci.* **2000**, *30*, 363–385.
- Casey, P.; Bogan, J.; McCoy, A.; Lozano, J. G.; Nellist, P. D.; Hughes, G. Chemical and structural investigations of the interactions of Cu with MnSiO₃ diffusion barrier layers. *J. Appl. Phys.* **2012**, *112*, 064507.
- Sun, H.; Qin, X.; Zaera, F. Chemical Nature of the Thin Films that Form on SiO₂/Si(100) Surfaces Upon Manganese Deposition. *J. Phys. Chem. Lett.* **2011**, *2*, 2525–2530.
- Matsumoto, K.; Neishi, K.; Itoh, H.; Sato, H.; Hosaka, S.; Koike, J. Chemical Vapor Deposition of Mn and Mn Oxide and their Step Coverage and Diffusion Barrier Properties on Patterned Interconnect Structures. *Appl. Phys. Express* **2009**, *2*, 036503.
- Moon, D. Y.; Han, D. S.; Park, J. H.; Shin, S. Y.; Park, J. W.; Kim, B. M.; Cho, J. Y. Plasma-enhanced atomic layer deposition of Cu-Mn films with formation of a MnSi_xO_y barrier layer. *Thin Solid Films* **2012**, *521*, 146–149.
- Kafizas, A.; Carmalt, C. J.; Parkin, I. P. CVD and precursor chemistry of transition metal nitrides. *Coord. Chem. Rev.* **2013**, *257*, 2073–2119.

- (12) McElwee-White, L. Design of Precursors for the CVD of Inorganic Thin Films. *Dalton Trans.* **2006**, 5327–5333.
- (13) McElwee-White, L.; Koller, J.; Kim, D.; Anderson, T. J. Mechanism-Based Design of Precursors for MOCVD. *ECS Trans.* **2009**, *25*, 161–171.
- (14) Winter, C. H.; Zheng, W.; El-Kaderi, H. M. Metallic Materials Deposition: Metal-Organic Precursors. In *Encyclopedia of Inorganic Chemistry*, 2nd ed.; Wiley: Chichester, U.K., 2005; Vol. 5, pp 3121–3144.
- (15) Bchir, O.; Green, K.; Hlad, M.; Anderson, T.; Brooks, B.; Wilder, C.; Powell, D.; McElwee-White, L. $\text{Cl}_4(\text{PhCN})\text{W}(\text{NPh})$ as a single-source MOCVD precursor for deposition of tungsten nitride (WN_x) thin films. *J. Organomet. Chem.* **2003**, *684*, 338–350.
- (16) Rische, D.; Parala, H.; Baunemann, A.; Thiede, T.; Fischer, R. Guanidinato-based precursors for MOCVD of metal nitrides (M_xN : M = Ta, W). *Surf. Coat. Technol.* **2007**, *201*, 9125–9130.
- (17) Ajmera, H. M.; Heitsch, A. T.; Bchir, O. J.; Norton, L. L.; Reitfort, D. P.; McElwee-White, L.; Anderson, T. J. Deposition of WN_xC_y Using the Allylimido Complexes $\text{Cl}_4(\text{RCN})\text{W}(\text{NC}_3\text{H}_5)$: Effect of NH_3 on Film Properties. *J. Electrochem. Soc.* **2008**, *155*, H829–H835.
- (18) Ajmera, H. M.; Anderson, T. J.; Koller, J.; McElwee-White, L.; Norton, D. P. Deposition of WN_xC_y thin films for diffusion barrier application using the dimethylhydrazido (2-) tungsten complex $(\text{CH}_3\text{CN})\text{Cl}_4\text{W}(\text{NNMe}_2)$. *Thin Solid Films* **2009**, *517*, 6038–6045.
- (19) Kim, D.; Kim, O. H.; Anderson, T.; Koller, J.; McElwee-White, L.; Leu, L. C.; Tsai, J. M.; Norton, D. P. Chemical vapor deposition of WN_xC_y using the tungsten piperidylhydrazido complex $\text{Cl}_4(\text{CH}_3\text{CN})\text{W}(\text{N-pip})$: Deposition, characterization, and diffusion barrier evaluation. *J. Vac. Sci. Technol., A* **2009**, *27*, 943–950.
- (20) Crane, E. L.; Chiu, H. T.; Nuzzo, R. G. Kinetic and mechanistic studies of the chemical vapor deposition of tungsten nitride from bis(tertbutylimido)bis(tertbutylamido)tungsten. *J. Phys. Chem. B* **2001**, *105*, 3549–3556.
- (21) Srinivasan, N. B.; Thiede, T. B.; de los Arcos, T.; Rogalla, D.; Becker, H. W.; Devi, A.; Fischer, R. A. MOCVD of tungsten nitride thin films: Comparison of precursor performance and film characteristics. *Phys. Status Solidi A* **2014**, *211*, 260–266.
- (22) Kim, H. Atomic layer deposition of metal and nitride thin films: Current research efforts and applications for semiconductor device processing. *J. Vac. Sci. Technol., B: Microelectron. Process. Phenom.* **2003**, *21*, 2231–2261.
- (23) Chatterjee, S.; Kuo, Y.; Lu, J. Thermal annealing effect on electrical properties of metal nitride gate electrodes with hafnium oxide gate dielectrics in nano-metric MOS devices. *Microelectron. Eng.* **2008**, *85*, 202–209.
- (24) Lu, J.; Kuo, Y.; Chatterjee, S.; Tewg, J. Physical and electrical properties of Ta-N, Mo-N, and W-N electrodes on HfO_2 high-k gate dielectric. *J. Vac. Sci. Technol., B* **2006**, *24*, 349–357.
- (25) Bchir, O.; Green, K.; Ajmera, H.; Zapp, E.; Anderson, T.; Brooks, B.; Reitfort, L.; Powell, D.; Abboud, K.; McElwee-White, L. Tungsten allylimido complexes $\text{Cl}_4(\text{RCN})\text{W}(\text{NC}_3\text{H}_5)$ as single-source CVD precursors for WN_xC_y thin films. Correlation of precursor fragmentation to film properties. *J. Am. Chem. Soc.* **2005**, *127*, 7825–7833.
- (26) Potts, S.; Carmalt, C.; Blackman, C.; Leese, T.; Davies, H. Tungsten imido complexes as precursors to tungsten carbonitride thin films. *Dalton Trans.* **2008**, 5730–5736.
- (27) Chiu, H. T.; Chuang, S. H. Tungsten Nitride Thin-Films Prepared By MOCVD. *J. Mater. Res.* **1993**, *8*, 1353–1360.
- (28) Gwilties, V.; Thiede, T. B.; Amirjalayer, S.; Alsamman, L.; Devi, A.; Fischer, R. A. All-Nitrogen Coordinated Amidinato/Imido Complexes of Molybdenum and Tungsten: Syntheses and Characterization. *Inorg. Chem.* **2010**, *49*, 8487–8494.
- (29) Koller, J.; Ajmera, H. M.; Abboud, K. A.; Anderson, T. J.; McElwee-White, L. Synthesis and Characterization of Diorganohydrazido(2-) Tungsten Complexes. *Inorg. Chem.* **2008**, *47*, 4457–4462.
- (30) McClain, K. R.; O'Donohue, C.; Shi, Z.; Walker, A. V.; Abboud, K. A.; Anderson, T.; McElwee-White, L. Synthesis of $\text{WN}(\text{NMe}_2)_3$ as a Precursor for the Deposition of WN_x Nanospheres. *Eur. J. Inorg. Chem.* **2012**, *2012*, 4579–4584.
- (31) McClain, K. R.; O'Donohue, C.; Koley, A.; Bonsu, R. O.; Abboud, K. A.; Revelli, J. C.; Anderson, T. J.; McElwee-White, L. Tungsten Nitrido Complexes as Precursors for Low Temperature Chemical Vapor Deposition of WN_xC_y Films as Diffusion Barriers for Cu Metallization. *J. Am. Chem. Soc.* **2014**, *136*, 1650–1662.
- (32) O'Donohue, C. T.; McClain, K. R.; Koley, A.; Revelli, J. C.; McElwee-White, L.; Anderson, T. J. Low Temperature Deposition of WN_xC_y Diffusion Barriers Using $\text{WN}(\text{NEt}_2)_3$ as a Single-Source Precursor. *ECS J. Solid State Sci. Technol.* **2015**, *4*, N3180–N3187.
- (33) Just, O.; Obi-Johnson, B.; Matthews, J.; Levermore, D.; Jones, T.; Rees, W. S., Jr. Design, synthesis, and characterization of precursors for chemical vapor deposition of oxide-based electronic materials. *MRS Online Proc. Libr.* **1999**, *606*, 3–12.
- (34) Hubert-Pfalzgraf, L. G.; Guillon, H. Trends in precursor design for conventional and aerosol-assisted CVD of high-Tc superconductors. *Appl. Organomet. Chem.* **1998**, *12*, 221–236.
- (35) Seligson, A. L.; Trogler, W. C. Cone Angles for Amine Ligands - X-Ray Crystal-Structures and Equilibrium Measurements for Ammonia, Ethylamine, Diethylamine, and Triethylamine Complexes with the (bis(dimethylphosphino)ethane)methylpalladium(II) Cation. *J. Am. Chem. Soc.* **1991**, *113*, 2520–2527.
- (36) Raaijmakers, I. J.; Yang, J. Low-Temperature MOCVD of Advanced Barrier Layers For the Microelectronics Industry. *Appl. Surf. Sci.* **1993**, *73*, 31–41.
- (37) Bchir, O. J.; Green, K. M.; Ajmera, H. M.; Zapp, E. A.; Anderson, T. J.; Brooks, B. C.; Reitfort, L. L.; Powell, D. H.; Abboud, K. A.; McElwee-White, L. The Tungsten Allylimido Complexes $\text{Cl}_4(\text{RCN})\text{W}(\text{NC}_3\text{H}_5)$ as Single-source CVD Precursors for WN_xC_y Thin Films. Correlation of Precursor Fragmentation to Film Properties. *J. Am. Chem. Soc.* **2005**, *127*, 7825–7833.
- (38) Smith, M. B.; March, J. *March's Advanced Organic Chemistry. Reactions, Mechanism and Structure*, 5th ed.; Wiley-Interscience: New York, 2001.
- (39) National Institute of Standards and Technology (NIST), Gaithersburg, MD, 2012.
- (40) Furimsky, E. Effect of catalyst surface on decomposition of nitrogen heterorings during regeneration of hydroprocessing catalysts. *Catal. Today* **1998**, *46*, 3–12.
- (41) Chen, H.; Yang, Y.; Huo, K. F.; Ma, Y. W.; Chen, Y.; Wang, X. S.; Lu, Y. N. Synergism of C_3N six-membered ring and vapor-liquid-solid growth of CN_x nanotubes with pyridine precursor. *J. Phys. Chem. B* **2006**, *110*, 16422–16427.
- (42) Matsuyama, T.; Tsubouchi, N.; Ohtsuka, Y. Catalytic decomposition of nitrogen-containing heterocyclic compounds with highly dispersed iron nanoparticles on carbons. *J. Mol. Catal. A: Chem.* **2012**, *356*, 14–19.
- (43) Davies, P. R.; Newton, N. G. The chemisorption and decomposition of pyridine and ammonia at clean and oxidized Al(111) surfaces. *Surf. Sci.* **2003**, *546*, 149–158.
- (44) Kreuzer, H. J. Theory of sticking: The effect of lateral interactions. *J. Chem. Phys.* **1996**, *104*, 9593–9612.
- (45) Tsetseris, L.; Logothetidis, S.; Pantelides, S. Atomic-scale mechanisms for diffusion of impurities in transition-metal nitrides. *Surf. Coat. Technol.* **2010**, *204*, 2089–2094.
- (46) Joint Committee on Powder Diffraction Standards (JCPDS), International Center for Diffraction Data, Swarthmore, PA, 1982, 1988.
- (47) Abisset, S.; Maury, F.; Ducarroir, M.; Nadal, M.; Andrieux, M.; Poirier, L.; Teyssandier, F. Nitriding pretreatments compatible with MOCVD and plasma CVD processes: influence on the adhesion of ceramic coatings on steel. *Ann. Chim.* **1998**, *23*, 707–720.
- (48) Abisset, S.; Maury, F. Low-temperature MOCVD of V-C-N coatings using bis(arene)vanadium as precursors. *Surf. Coat. Technol.* **1998**, *108–109*, 200–205.